



CHORUS

This is the accepted manuscript made available via CHORUS. The article has been published as:

Experimental study of ψ^{\prime} decays to $K^{+}K^{-}\pi^{0}$ and $K^{+}K^{-}\eta$

M. Ablikim *et al.* (BESIII Collaboration)

Phys. Rev. D **86**, 072011 — Published 26 October 2012

DOI: [10.1103/PhysRevD.86.072011](https://doi.org/10.1103/PhysRevD.86.072011)

Experimental study of ψ' decays to $K^+K^-\pi^0$ and $K^+K^-\eta$

M. Ablikim¹, M. N. Achasov⁵, O. Albayrak³, D. J. Ambrose³⁹, F. F. An¹, Q. An⁴⁰,
J. Z. Bai¹, Y. Ban²⁷, J. Becker², J. V. Bennett¹⁷, M. Bertani^{18A}, J. M. Bian³⁸, E. Boger^{20,a},
O. Bondarenko²¹, I. Boyko²⁰, R. A. Briere³, V. Bytev²⁰, X. Cai¹, O. Cakir^{35A}, A. Calcaterra^{18A},
G. F. Cao¹, S. A. Cetin^{35B}, J. F. Chang¹, G. Chelkov^{20,a}, G. Chen¹, H. S. Chen¹, J. C. Chen¹,
M. L. Chen¹, S. J. Chen²⁵, Y. B. Chen¹, H. P. Cheng¹⁴, Y. P. Chu¹, D. Cronin-Hennessy³⁸,
H. L. Dai¹, J. P. Dai¹, D. Dedovich²⁰, Z. Y. Deng¹, A. Denig¹⁹, I. Denysenko^{20,b},
M. Destefanis^{43A,43C}, W. M. Ding²⁹, Y. Ding²³, L. Y. Dong¹, M. Y. Dong¹, S. X. Du⁴⁶, J. Fang¹,
S. S. Fang¹, L. Fava^{43B,43C}, F. Feldbauer², C. Q. Feng⁴⁰, R. B. Feroli^{18A}, C. D. Fu¹, J. L. Fu²⁵,
Y. Gao³⁴, C. Geng⁴⁰, K. Goetzen⁷, W. X. Gong¹, W. Gradl¹⁹, M. Greco^{43A,43C}, M. H. Gu¹,
Y. T. Gu⁹, Y. H. Guan⁶, A. Q. Guo²⁶, L. B. Guo²⁴, Y. P. Guo²⁶, Y. L. Han¹, F. A. Harris³⁷,
K. L. He¹, M. He¹, Z. Y. He²⁶, T. Held², Y. K. Heng¹, Z. L. Hou¹, H. M. Hu¹, T. Hu¹,
G. M. Huang¹⁵, G. S. Huang⁴⁰, J. S. Huang¹², X. T. Huang²⁹, Y. P. Huang¹, T. Hussain⁴²,
C. S. Ji⁴⁰, Q. Ji¹, Q. P. Ji^{26,c}, X. B. Ji¹, X. L. Ji¹, L. L. Jiang¹, X. S. Jiang¹, J. B. Jiao²⁹,
Z. Jiao¹⁴, D. P. Jin¹, S. Jin¹, F. F. Jing³⁴, N. Kalantar-Nayestanaki²¹, M. Kavatsyuk²¹,
W. Kuehn³⁶, W. Lai¹, J. S. Lange³⁶, C. H. Li¹, Cheng Li⁴⁰, Cui Li⁴⁰, D. M. Li⁴⁶, F. Li¹,
G. Li¹, H. B. Li¹, J. C. Li¹, K. Li¹⁰, Lei Li¹, Q. J. Li¹, S. L. Li¹, W. D. Li¹, W. G. Li¹,
X. L. Li²⁹, X. N. Li¹, X. Q. Li²⁶, X. R. Li²⁸, Z. B. Li³³, H. Liang⁴⁰, Y. F. Liang³¹, Y. T. Liang³⁶,
G. R. Liao³⁴, X. T. Liao¹, B. J. Liu¹, C. L. Liu³, C. X. Liu¹, C. Y. Liu¹, F. H. Liu³⁰, Fang Liu¹,
Feng Liu¹⁵, H. Liu¹, H. H. Liu¹³, H. M. Liu¹, H. W. Liu¹, J. P. Liu⁴⁴, K. Y. Liu²³, Kai Liu⁶,
P. L. Liu²⁹, Q. Liu⁶, S. B. Liu⁴⁰, X. Liu²², Y. B. Liu²⁶, Z. A. Liu¹, Zhiqiang Liu¹, Zhiqing Liu¹,
H. Loehner²¹, G. R. Lu¹², H. J. Lu¹⁴, J. G. Lu¹, Q. W. Lu³⁰, X. R. Lu⁶, Y. P. Lu¹, C. L. Luo²⁴,
M. X. Luo⁴⁵, T. Luo³⁷, X. L. Luo¹, M. Lv¹, C. L. Ma⁶, F. C. Ma²³, H. L. Ma¹, Q. M. Ma¹,
S. Ma¹, T. Ma¹, X. Y. Ma¹, Y. Ma¹¹, F. E. Maas¹¹, M. Maggiora^{43A,43C}, Q. A. Malik⁴²,
Y. J. Mao²⁷, Z. P. Mao¹, J. G. Messchendorp²¹, J. Min¹, T. J. Min¹, R. E. Mitchell¹⁷, X. H. Mo¹,
C. Morales Morales¹¹, C. Motzko², N. Yu. Muchnoi⁵, H. Muramatsu³⁹, Y. Nefedov²⁰,
C. Nicholson⁶, I. B. Nikolaev⁵, Z. Ning¹, S. L. Olsen²⁸, Q. Ouyang¹, S. Pacetti^{18B}, J. W. Park²⁸,
M. Pelizaeus³⁷, H. P. Peng⁴⁰, K. Peters⁷, J. L. Ping²⁴, R. G. Ping¹, R. Poling³⁸, E. Prencipe¹⁹,

M. Qi²⁵, S. Qian¹, C. F. Qiao⁶, X. S. Qin¹, Y. Qin²⁷, Z. H. Qin¹, J. F. Qiu¹, K. H. Rashid⁴²,
G. Rong¹, X. D. Ruan⁹, A. Sarantsev^{20,d}, B. D. Schaefer¹⁷, J. Schulze², M. Shao⁴⁰, C. P. Shen^{37,e},
X. Y. Shen¹, H. Y. Sheng¹, M. R. Shepherd¹⁷, X. Y. Song¹, S. Spataro^{43A,43C}, B. Spruck³⁶,
D. H. Sun¹, G. X. Sun¹, J. F. Sun¹², S. S. Sun¹, Y. J. Sun⁴⁰, Y. Z. Sun¹, Z. J. Sun¹, Z. T. Sun⁴⁰,
C. J. Tang³¹, X. Tang¹, I. Tapan^{35C}, E. H. Thorndike³⁹, D. Toth³⁸, M. Ullrich³⁶, G. S. Varner³⁷,
B. Wang⁹, B. Q. Wang²⁷, K. Wang¹, L. L. Wang¹, L. S. Wang¹, M. Wang²⁹, P. Wang¹,
P. L. Wang¹, Q. Wang¹, Q. J. Wang¹, S. G. Wang²⁷, X. L. Wang⁴⁰, Y. D. Wang⁴⁰, Y. F. Wang¹,
Y. Q. Wang²⁹, Z. Wang¹, Z. G. Wang¹, Z. Y. Wang¹, D. H. Wei⁸, P. Weidenkaff¹⁹, Q. G. Wen⁴⁰,
S. P. Wen¹, M. Werner³⁶, U. Wiedner², L. H. Wu¹, N. Wu¹, S. X. Wu⁴⁰, W. Wu²⁶, Z. Wu¹,
L. G. Xia³⁴, Z. J. Xiao²⁴, Y. G. Xie¹, Q. L. Xiu¹, G. F. Xu¹, G. M. Xu²⁷, H. Xu¹, Q. J. Xu¹⁰,
X. P. Xu³², Z. R. Xu⁴⁰, F. Xue¹⁵, Z. Xue¹, L. Yan⁴⁰, W. B. Yan⁴⁰, Y. H. Yan¹⁶, H. X. Yang¹,
Y. Yang¹⁵, Y. X. Yang⁸, H. Ye¹, M. Ye¹, M. H. Ye⁴, B. X. Yu¹, C. X. Yu²⁶, J. S. Yu²²,
S. P. Yu²⁹, C. Z. Yuan¹, Y. Yuan¹, A. A. Zafar⁴², A. Zallo^{18A}, Y. Zeng¹⁶, B. X. Zhang¹,
B. Y. Zhang¹, C. Zhang²⁵, C. C. Zhang¹, D. H. Zhang¹, H. H. Zhang³³, H. Y. Zhang¹,
J. Q. Zhang¹, J. W. Zhang¹, J. Y. Zhang¹, J. Z. Zhang¹, S. H. Zhang¹, X. J. Zhang¹,
X. Y. Zhang²⁹, Y. Zhang¹, Y. H. Zhang¹, Y. S. Zhang⁹, Z. P. Zhang⁴⁰, Z. Y. Zhang⁴⁴, G. Zhao¹,
H. S. Zhao¹, J. W. Zhao¹, K. X. Zhao²⁴, Lei Zhao⁴⁰, Ling Zhao¹, M. G. Zhao²⁶, Q. Zhao¹,
Q. Z. Zhao^{9,f}, S. J. Zhao⁴⁶, T. C. Zhao¹, X. H. Zhao²⁵, Y. B. Zhao¹, Z. G. Zhao⁴⁰,
A. Zhemchugov^{20,a}, B. Zheng⁴¹, J. P. Zheng¹, Y. H. Zheng⁶, B. Zhong¹, J. Zhong², Z. Zhong^{9,f},
L. Zhou¹, X. K. Zhou⁶, X. R. Zhou⁴⁰, C. Zhu¹, K. Zhu¹, K. J. Zhu¹, S. H. Zhu¹, X. L. Zhu³⁴,
Y. C. Zhu⁴⁰, Y. M. Zhu²⁶, Y. S. Zhu¹, Z. A. Zhu¹, J. Zhuang¹, B. S. Zou¹, J. H. Zou¹

(BESIII Collaboration)

¹ *Institute of High Energy Physics, Beijing 100049, P. R. China*

² *Bochum Ruhr-University, 44780 Bochum, Germany*

³ *Carnegie Mellon University, Pittsburgh, PA 15213, USA*

⁴ *China Center of Advanced Science and Technology, Beijing 100190, P. R. China*

⁵ *G.I. Budker Institute of Nuclear Physics SB RAS (BINP), Novosibirsk 630090, Russia*

⁶ *Graduate University of Chinese Academy of Sciences, Beijing 100049, P. R. China*

⁷ *GSI Helmholtzcentre for Heavy Ion Research GmbH, D-64291 Darmstadt, Germany*

⁸ *Guangxi Normal University, Guilin 541004, P. R. China*

- ⁹ *GuangXi University, Nanning 530004, P.R.China*
- ¹⁰ *Hangzhou Normal University, Hangzhou 310036, P. R. China*
- ¹¹ *Helmholtz Institute Mainz, J.J. Becherweg 45, D 55099 Mainz, Germany*
- ¹² *Henan Normal University, Xinxiang 453007, P. R. China*
- ¹³ *Henan University of Science and Technology, Luoyang 471003, P. R. China*
- ¹⁴ *Huangshan College, Huangshan 245000, P. R. China*
- ¹⁵ *Huazhong Normal University, Wuhan 430079, P. R. China*
- ¹⁶ *Hunan University, Changsha 410082, P. R. China*
- ¹⁷ *Indiana University, Bloomington, Indiana 47405, USA*
- ¹⁸ *(A)INFN Laboratori Nazionali di Frascati, Frascati, Italy;*
(B)INFN and University of Perugia, I-06100, Perugia, Italy
- ¹⁹ *Johannes Gutenberg University of Mainz,*
Johann-Joachim-Becher-Weg 45, 55099 Mainz, Germany
- ²⁰ *Joint Institute for Nuclear Research, 141980 Dubna, Russia*
- ²¹ *KVI/University of Groningen, 9747 AA Groningen, The Netherlands*
- ²² *Lanzhou University, Lanzhou 730000, P. R. China*
- ²³ *Liaoning University, Shenyang 110036, P. R. China*
- ²⁴ *Nanjing Normal University, Nanjing 210046, P. R. China*
- ²⁵ *Nanjing University, Nanjing 210093, P. R. China*
- ²⁶ *Nankai University, Tianjin 300071, P. R. China*
- ²⁷ *Peking University, Beijing 100871, P. R. China*
- ²⁸ *Seoul National University, Seoul, 151-747 Korea*
- ²⁹ *Shandong University, Jinan 250100, P. R. China*
- ³⁰ *Shanxi University, Taiyuan 030006, P. R. China*
- ³¹ *Sichuan University, Chengdu 610064, P. R. China*
- ³² *Soochow University, Suzhou 215006, China*
- ³³ *Sun Yat-Sen University, Guangzhou 510275, P. R. China*
- ³⁴ *Tsinghua University, Beijing 100084, P. R. China*
- ³⁵ *(A)Ankara University, Ankara, Turkey; (B)Dogus University,*
Istanbul, Turkey; (C)Uludag University, Bursa, Turkey
- ³⁶ *Universitaet Giessen, 35392 Giessen, Germany*

³⁷ *University of Hawaii, Honolulu, Hawaii 96822, USA*

³⁸ *University of Minnesota, Minneapolis, MN 55455, USA*

³⁹ *University of Rochester, Rochester, New York 14627, USA*

⁴⁰ *University of Science and Technology of China, Hefei 230026, P. R. China*

⁴¹ *University of South China, Hengyang 421001, P. R. China*

⁴² *University of the Punjab, Lahore-54590, Pakistan*

⁴³ *(A)University of Turin, Turin, Italy; (B)University of Eastern Piedmont, Alessandria, Italy; (C)INFN, Turin, Italy*

⁴⁴ *Wuhan University, Wuhan 430072, P. R. China*

⁴⁵ *Zhejiang University, Hangzhou 310027, P. R. China*

⁴⁶ *Zhengzhou University, Zhengzhou 450001, P. R. China*

^a *also at the Moscow Institute of Physics and Technology, Moscow, Russia*

^b *on leave from the Bogolyubov Institute for Theoretical Physics, Kiev, Ukraine*

^c *Nankai University, Tianjin, 300071, China*

^d *also at the PNPI, Gatchina, Russia*

^e *now at Nagoya University, Nagoya, Japan*

^f *Guangxi University, Nanning, 530004, China*

Abstract

Using $(106 \pm 4) \times 10^6$ ψ' events accumulated with the BESIII detector at the BEPCII e^+e^- collider, we present measurements of the branching fractions for ψ' decays to $K^+K^-\pi^0$ and $K^+K^-\eta$. In these final states, the decay $\psi' \rightarrow K_2^*(1430)^+K^- + c.c.$ is observed for the first time, and its branching fraction is measured to be $(7.12 \pm 0.62 \text{ (stat.)}_{-0.61}^{+1.13} \text{ (syst.)}) \times 10^{-5}$, which indicates a violation of the helicity selection rule in ψ' decays. The branching fractions of $\psi' \rightarrow K^*(892)^+K^- + c.c.$, $\phi\eta$, $\phi\pi^0$ are also measured. The measurements are used to test the QCD predictions on charmonium decays.

PACS numbers: 13.25.Gv, 13.20.Gd, 14.40.Pq

I. INTRODUCTION

In the framework of perturbative QCD (pQCD), J/ψ and ψ' decays to light hadrons are expected to be dominated by the annihilation of $c\bar{c}$ quarks into three gluons or one virtual photon, with hadron decay partial widths that are proportional to the square of the $c\bar{c}$ wave function overlaps at the origin, which can be related to their leptonic decay widths [1]. This suggests that the ratio Q_h of branching fractions for ψ' and J/ψ decays to the same final state should follow the rule:

$$Q_h = \frac{Br(\psi' \rightarrow h)}{Br(J/\psi \rightarrow h)} \cong \frac{Br(\psi' \rightarrow e^+e^-)}{Br(J/\psi \rightarrow e^+e^-)} \cong 12\%, \quad (1)$$

where Br denotes a branching fraction and h is a particular hadronic final state. This relation is referred to as the “12% rule”.

Although the 12% rule works well for some specific decay modes of the ψ' , the decay ψ' to $\rho\pi$ exhibits a factor of 70 times stronger suppression than expectations based on this rule. This suppression in vector-pseudoscalar (VP) meson modes was first observed by MARKII [2], which is referred to as the “ $\rho\pi$ puzzle”. Further tests of this rule in the VP modes have been performed by CLEO [3] and BESII [4], and have been extended to the pseudoscalar-pseudoscalar meson (PP), vector-tensor meson (VT) and multibody decays. Although Q_h values have been measured for a wide variety of final states, most of them have large uncertainties due to low statistics [5]. Reviews of the rho-pi puzzle conclude that current theoretical explanations are unsatisfactory [6]. More experimental results are desirable.

For charmonium $\psi(\lambda)$ decays to light hadrons $h_1(\lambda_1)$ and $h_2(\lambda_2)$, the asymptotic behavior of the branching fraction from a pQCD calculation to leading twist accuracy gives [7]:

$$Br[\psi(\lambda) \rightarrow h_1(\lambda_1)h_2(\lambda_2)] \sim \left(\frac{\Lambda_{\text{QCD}}^2}{m_c^2} \right)^{|\lambda_1+\lambda_2|+2}, \quad (2)$$

where λ , λ_1 and λ_2 denote the helicities of the corresponding hadrons. Here m_c is the charm quark mass and Λ_{QCD} is the QCD energy scale factor. If the light quark masses are neglected, the vector-gluon coupling conserves quark helicity and this leads to the helicity selection rule (HSR) [8]: $\lambda_1 + \lambda_2 = 0$. If the helicity configurations do not satisfy this relation, the branching fraction should be suppressed.

For the ψ' decays to VP [$K^*(892)^\pm K^\mp$] or TP [$K_2^*(1430)^\pm K^\mp$], the amplitudes are anti-symmetric in terms of the final state helicities, since strong or electromagnetic interactions conserve parity. Hence the amplitudes vanish when $\lambda_1 = \lambda_2 = 0$. Nonvanishing amplitudes require the helicity configuration to satisfy the relation $|\lambda_1 + \lambda_2| = 1$, which violates the HSR and the branching fractions are expected to be suppressed.

Strikingly, HSR-violating decays were recently observed in χ_{cJ} decays into vector-vector meson pairs by BESIII [9], which strongly indicates the failure of the HSR [10]. In an analysis of $\psi' \rightarrow K_S^0 K^\pm \pi^\mp$ by BESII [4], evidence for $\psi' \rightarrow K_J^* K^0$ (K_J^* refers to either $K_J^*(1430)$ or $K^*(1410)$) was seen, but low statistics prevented a further study.

With the large ψ' data sample accumulated by the BESIII experiment, new opportunities to precisely test the 12% rule in the decays of $\psi' \rightarrow K^*(892)^+ K^- + c.c.$ and $\eta\phi$, and to search for $\psi' \rightarrow K_2^*(1430)^\pm K^\mp$ are available. Such measurements can shed light on charmonium decay mechanisms and, therefore, be helpful for understanding the $\rho\pi$ puzzle. In particular, the decay $\psi' \rightarrow K^+ K^- \eta$ provides opportunities to study not only $\phi\eta$, but also the excited ϕ states, such as $\phi_3(1850)$ and $\phi(2170)$. The decay $\psi' \rightarrow K^+ K^- \pi^0$ also allows us to study the isospin violation decay $\psi' \rightarrow \phi\pi^0$, which is expected to proceed via electromagnetic (EM) processes [11].

II. THE BESIII EXPERIMENT AND DATA SET

We use a data sample containing $(106 \pm 4) \times 10^6$ ψ' decays recorded with the BESIII detector [12] at the energy-symmetric double ring e^+e^- collider BEPCII. The primary data sample corresponds to an integrated luminosity of 156.4 pb^{-1} collected at the peak of the ψ' resonance. In addition, a 2.9 fb^{-1} (43 pb^{-1}) data sample collected at a center-of-mass energy of 3.773 GeV (3.65 GeV) is used for continuum background studies.

BEPCII is designed to provide a peak luminosity of $10^{33} \text{ cm}^{-2}\text{s}^{-1}$ at a beam current of 0.93 A for studies of hadron spectroscopy and τ -charm physics [13]. The BESIII detector is described in detail elsewhere [12]. Charged particle momenta are measured with a small-celled, helium-gas-based main drift chamber (MDC) with 43 layers operating within the 1T magnetic field of a solenoidal superconducting magnet. Charged particle identification is provided by measurements of the specific ionization energy loss dE/dx in the tracking device

and by means of a plastic scintillator time of flight (TOF) system comprised of a barrel part and two endcaps. Photons are detected and their energies and positions measured with an electromagnetic calorimeter (EMC) consisting of 6240 CsI(Tl) crystals arranged in a barrel and two endcaps. The return yoke of the magnet is instrumented with resistive plate chambers arranged in 9 (barrel) and 8 layers (endcaps) for the discrimination of muons and charged hadrons.

The optimization of the event selection criteria and the estimation of background sources are performed with Monte Carlo (MC) simulated data samples. The GEANT4-based simulation software [14] includes the geometric and material description of the BESIII detectors, the detector response and digitization models, as well as the tracking of the detector running conditions and performances. An inclusive ψ' MC sample is generated to study potential backgrounds. The production of the ψ' resonance is simulated with the MC event generator KKMC [15], while the decays are generated with BESEVTGEN [16] for known decay modes with branching fractions being set at their PDG [5] world average values, and with LUNDCHARM [17] for the remaining unknown decays. The analysis is performed in the framework of the BESIII offline software system [18] which provides the detector calibration, event reconstruction and data storage.

III. EVENT SELECTION

The selection criteria described below are similar to those used in previous BESIII analyses [9, 19] and are optimized according to the signal significance.

A. Photon identification

Electromagnetic showers are reconstructed by clustering EMC crystal energies. The energy deposited in nearby TOF counters is included to improve the reconstruction efficiency and the energy resolution. Shower identified as photon candidates must satisfy fiducial and shower-quality requirements. Photon candidates that are reconstructed from the barrel region ($|\cos\theta| < 0.8$) must have a minimum energy of 25 MeV, while those in the endcaps ($0.86 < |\cos\theta| < 0.92$) must have at least 50 MeV. Showers in the angular range between the barrel and endcap are poorly reconstructed and excluded from the analysis. To eliminate

showers caused by bremsstrahlung charged particles, a photon must be separated by at least 10° from any charged track. EMC cluster timing requirements are used to suppress electronic noise and energy deposits from uncorrelated events. The number of photon candidates N_γ is required to be $2 \leq N_\gamma \leq 10$.

B. Charged particle identification

Charged tracks are reconstructed from hits in the MDC. For each track, the polar angle must satisfy $|\cos \theta| < 0.93$, and it must originate within ± 10 cm from the interaction point in the beam direction and within ± 1 cm of the beam line in the plane perpendicular to the beam. The number of charged tracks is required to be two with a net charge of zero. The time-of-flight and energy loss dE/dx measurements are combined to calculate particle identification (PID) probabilities for pion, kaon, and proton/antiproton hypotheses, and each track is assigned a particle type corresponding to the hypothesis with the highest confidence level. Both charged tracks are required to be identified as kaons.

C. Event selection criteria

To choose the correct $\gamma\gamma$ combination for the π^0 or η identification and to improve the overall mass resolution, a four-constraint kinematic fit (4C-fit) is applied under the hypothesis $\psi' \rightarrow \gamma\gamma K^+ K^-$ constrained to the sum of the initial e^+e^- beam four-momentum. For events with more than two photon candidates, the combination with the smallest χ^2 is kept. Candidates with $\chi^2 \leq 20$ for this fit are retained for further analysis. Figure 1 shows the invariant mass distribution for the two selected photons. Signal candidates of π^0 and η mesons are clearly seen.

1. Final selection of $\psi' \rightarrow K^+ K^- \pi^0$

Candidates π^0 are selected by requiring the invariant mass of two photons, $M_{\gamma\gamma}$, to satisfy the condition $0.117 \text{ GeV}/c^2 \leq M_{\gamma\gamma} \leq 0.147 \text{ GeV}/c^2$, an interval that is six times the π^0 mass resolution ($\sim 5 \text{ MeV}/c^2$). To suppress the background from $\psi' \rightarrow \gamma\chi_{c0}$, with $\chi_{c0} \rightarrow K^+ K^-$, it is required that the energy of the less energetic photon ($E_{\gamma_{low}}$) is larger than 70 MeV.

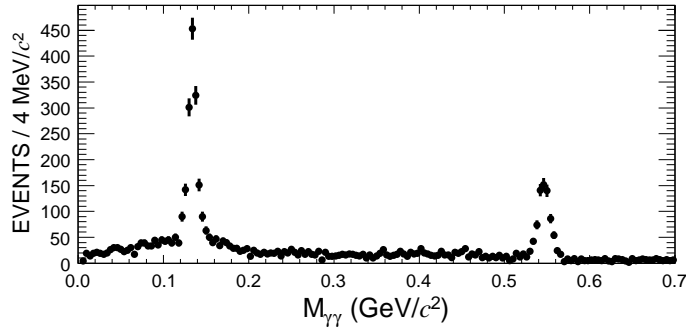


FIG. 1: The invariant mass distribution for two photons in the selected $\psi' \rightarrow \gamma\gamma K^+ K^-$ events.

Background events from $\psi' \rightarrow \pi^0 J/\psi$, with $J/\psi \rightarrow K^+ K^-$, are removed by requiring that the mass of the two kaons satisfies $|M_{K^+ K^-} - m_{J/\psi}| \geq 7 \text{ MeV}/c^2$, where $m_{J/\psi}$ is the J/ψ mass [5].

There are in total 1158 $\psi' \rightarrow K^+ K^- \pi^0$ events selected from the data. A Dalitz plot of these events is shown in Fig. 2. Invariant mass spectra of $\pi^0 K^\pm$ and $K^+ K^-$ are shown in Fig. 3. The two peaks in the $\pi^0 K^\pm$ mass spectrum correspond to the $K^*(892)^\pm$ and $K_j^{*\pm}$, where K_j^* may be $K_j^*(1430)$ or $K^*(1410)$. A partial wave analysis (PWA), described below, is used to study the Dalitz plot structures.

2. Final selection of $\psi' \rightarrow K^+ K^- \eta$

The η candidates are reconstructed using the two selected photons in $\gamma\gamma K^+ K^-$, and the η yields are determined by a fit to the $M_{\gamma\gamma}$ distribution. To suppress the background from $\psi' \rightarrow \eta J/\psi$, with $J/\psi \rightarrow K^+ K^-$, the invariant mass of the two kaons is required to be less than $3.05 \text{ GeV}/c^2$. The background from the decay $\psi' \rightarrow \gamma\chi_{c0/2}$, with $\chi_{c0/2} \rightarrow \pi^0/\eta K^+ K^-$ ($\chi_{c1} \rightarrow \pi^0 K^+ K^-$ or $\eta K^+ K^-$ is forbidden), is suppressed by requiring that the lower energy photon should be outside of the range 115 MeV to 185 MeV. A Dalitz plot of the surviving events is shown in Fig. 4, which is produced by using a loose η mass requirement of $0.48 \text{ GeV}/c^2 \leq M_{\gamma\gamma} \leq 0.6 \text{ GeV}/c^2$ compared to the mass resolution for $\eta \rightarrow \gamma\gamma$ ($\sim 7 \text{ MeV}/c^2$). The diagonal band shows a clean signal for $\psi' \rightarrow \phi\eta$ decays.

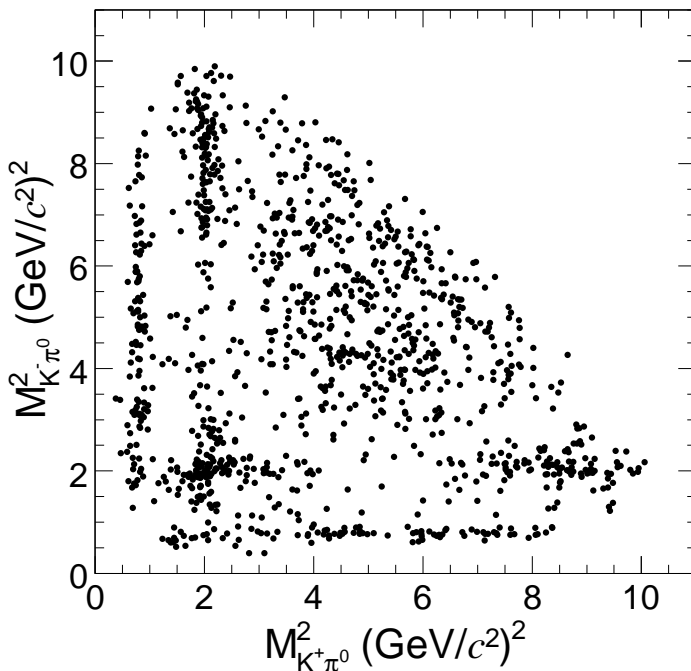


FIG. 2: The Dalitz plot for $\psi' \rightarrow K^+K^-\pi^0$.

IV. PARTIAL WAVE ANALYSIS OF $\psi' \rightarrow K^+K^-\pi^0$

We perform a partial wave analysis of the decay $\psi' \rightarrow K^+K^-\pi^0$ in order to determine branching fractions for $\psi' \rightarrow K^*(892)^\pm K^\mp$ and $K_J^{*\pm} K^\mp$.

A. The method

The method of the PWA is similar to that utilized in a previous BES publication [20]. The decay amplitudes are constructed using the relativistic covariant tensor amplitudes as described in Ref. [21]. For the decay $\psi' \rightarrow K^+K^-\pi^0$, the general form of amplitude reads:

$$A(m) = \psi_\mu(m)A^\mu = \psi_\mu(m) \sum_i \Lambda_i U_i^\mu, \quad (3)$$

where $\psi_\mu(m)$ is the polarization vector of ψ' with a helicity value m ; U_i^μ is the i -th partial-wave amplitude with the coupling strength determined by a complex parameter Λ_i . The differential cross section is given by

$$\frac{d\sigma}{d\Phi} = \frac{1}{2} \sum_{m=\pm 1} A^\mu(m)A^{*\mu}(m) = \sum_{m,i,j} P_{ij} \cdot F_{ij}, \quad (4)$$

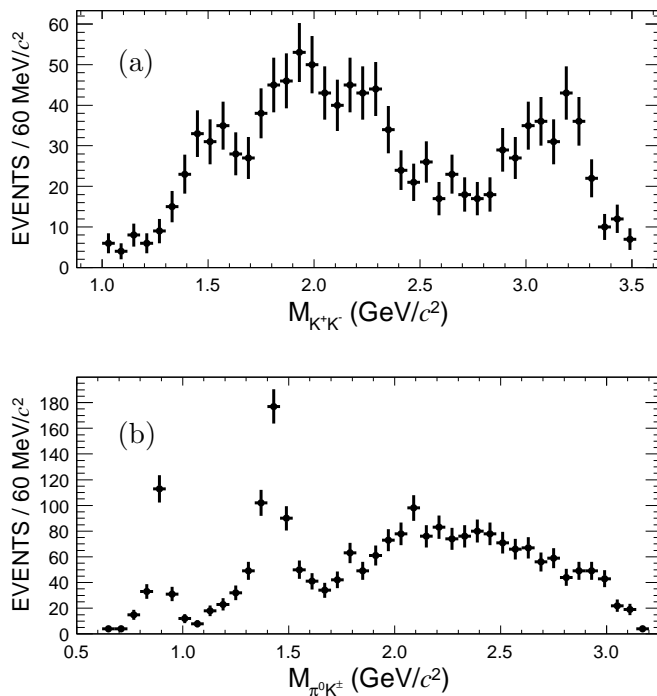


FIG. 3: The invariant mass projection of the Dalitz plot (see Fig. 3) for the $\psi' \rightarrow K^+K^-\pi^0$ decay. (a) $M_{K^+K^-}$ is plotted with one entry per event, and (b) $M_{\pi^0K^\pm}$ is plotted with two entries per event.

where $P_{ij} = P_{ji}^* \equiv \Lambda^i \Lambda^{*j}$ and $F_{ij} = F_{ji}^* \equiv \frac{1}{2} \sum_{\mu=1}^2 U_i^\mu U_j^{*\mu}$. Here, the sum over the ψ' polarization is taken as $m = \pm 1$ since the ψ' particle is produced from e^+e^- annihilation. The partial wave amplitudes U_i for the intermediate states, e.g. $K^*(892)^\pm K^\mp$, $K_2^*(1430)^\pm K^\mp$ etc., are constructed from the K^+ , K^- and π^0 four-momenta. In the amplitude, the line shape for the resonance is described with a Breit-Wigner function:

$$BW(s) = \frac{1}{M^2 - s - iM\Gamma}, \quad (5)$$

where s is the invariant-mass squared, and M and Γ represent the mass and width, respectively.

The relative magnitudes and phases for amplitudes U_i are determined by an unbinned maximum likelihood fit. The joint probability density for observing the N events in the data sample is

$$\mathcal{L} = \prod_{i=1}^N P(x_i), \quad (6)$$

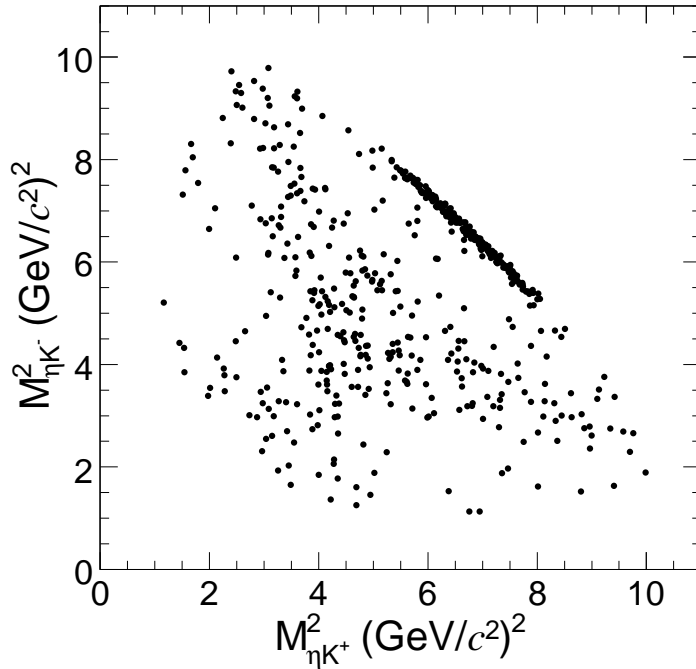


FIG. 4: The Dalitz plot for $\psi' \rightarrow \eta K^+ K^-$.

where $P(x_i)$ is a probability to produce event i with four-vector momentum $x_i = (p_{K^+}, p_{K^-}, p_{\pi^0})_i$. The normalized $P(x_i)$ is calculated from the differential cross section

$$P(x_i) = \frac{(d\sigma/d\Phi)_i}{\sigma_{MC}}, \quad (7)$$

where the normalization factor σ_{MC} is calculated from a MC sample with N_{MC} accepted events, which are generated with a phase space model and then subject to the detector simulation, and are passed through the same event selection criteria as applied to the data analysis. With an MC sample of sufficiently large size, the σ_{MC} is evaluated with

$$\sigma_{MC} = \frac{1}{N_{MC}} \sum_{i=1}^{N_{MC}} \left(\frac{d\sigma}{d\Phi} \right)_i. \quad (8)$$

For technical reasons, rather than maximizing \mathcal{L} , $S = -\ln \mathcal{L}$ is minimized using the package FUMILI [22].

B. Background subtraction

The number of non- π^0 background events in the selected $K^+ K^- \pi^0$ data sample, estimated from a π^0 sideband defined by $M_{\gamma\gamma} \in [0.079, 0.109]$ and $[0.165, 0.195]$ GeV/c^2 , is 43 ± 7

events. The MC simulation shows that these background events are mainly due to $\psi' \rightarrow \gamma\chi_{cJ}$, $\chi_{cJ} \rightarrow \gamma K^+ K^-$ or $\pi^0 K^+ K^-$. A low level of non- $K^+ K^-$ background (3 events) comes from $\psi' \rightarrow \pi^0 \pi^0 J/\psi$, $J/\psi \rightarrow \mu^+ \mu^-$ due to a misidentification of muons as kaons.

Events from the QED process, $e^+ e^- \rightarrow \gamma^* \rightarrow K^+ K^- \pi^0$ produced at a center-of-mass energy corresponding to the mass of the ψ' peak, have the same final state as our signals of interest. Background from this source is estimated from two data sets taken at $\sqrt{s} = 3.773$ GeV and 3.65 GeV. Since the decay of $\psi(3770) \rightarrow K^+ K^- \pi^0$ is not observed [5], the events obtained at $\sqrt{s} = 3.773$ GeV are regarded as all due to the QED process. After normalizing their integrated luminosities to that of the ψ' sample, the number of events obtained at each of the data sets are 195 ± 3 and 195 ± 27 , respectively, and in good agreement with each other.

The QED background events at the ψ' peak are generated using a model determined by performing a PWA fit to the data set taken at 3.773 GeV. As a cross check, the model with the determined coupling strengths is used to generate MC samples and compared with the data set taken at 3.650 GeV. Figure 5 compares mass distributions obtained from MC events with those obtained from experimental data. Here MC and experimental data were generated or taken at $\sqrt{s} = 3.650$ GeV. For the $K^+ K^-$ and $K \pi^0$ invariant mass distributions, the data and MC agree well within statistical errors, and a peak around $M_{\pi^0 K^\pm} = 1.4$ GeV/ c^2 can be seen.

In the PWA fit, background events obtained from MC simulation or π^0 mass sideband are used to account for the background events in the data using a negative log-likelihood value. Hence, the complete log-likelihood function is:

$$\ln \mathcal{L} = \ln \mathcal{L}_{dt} - \sum \ln \mathcal{L}_{bg}, \quad (9)$$

where \mathcal{L}_{dt} and \mathcal{L}_{bg} are the likelihoods determined with the data and background events, respectively. The backgrounds are divided into two kinds: reducible background and irreducible background (QED background). This technique of background treatment assumes no interference between signal and irreducible background events. This method has been used in the analysis of Crystal Barrel data [23] and BESII data [20, 24].

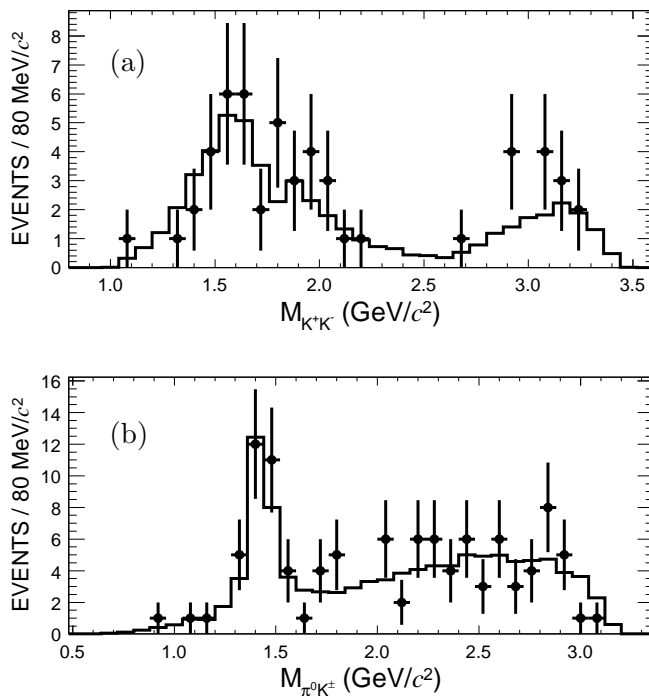


FIG. 5: The K^+K^- (one entry per event) and $K\pi$ (two entries per event) invariant mass distributions at $\sqrt{s} = 3.65$ GeV. The dots with error bars are data and the histograms are MC events as described in the text.

C. Analysis results

Motivated by the structures seen in the Dalitz plot (Fig. 2) and its projections (Fig. 3), the decay modes listed in Tables I and II are considered in the PWA fit. Only the modes with a statistical significance larger than 5 standard deviation (σ) are taken as the best solution, which includes the resonances $K^*(892)^\pm$, $K_2^*(1430)^\pm$, $K^*(1680)^\pm$ and $\rho(1700)$, and the non-resonance mode $K^+K^-\pi^0$ (see Table I). The significance of a mode is calculated by comparing the difference of the $S(= -\ln \mathcal{L})$ values between the fit with and without that mode. The non-resonance mode is described as a P -wave K^+K^- system. For the charge-conjugate channels, the coupling strengths in amplitudes are the same. Each mode in the amplitude introduces two parameters are determined by the PWA fit, the magnitude of the coupling strength and the phase angle.

Other intermediate states, like $\rho(770)$, $\rho(1450)$, $\rho(1900)$, $\rho(2150)$ in the K^+K^- final states, and $K^*(1410)^\pm$ and $K^*(1980)^\pm$ in the $\pi^0 K^\pm$ final states, were considered and tested in the

PWA fit. Adding them to the best solution does improve the fit quality, but these additional modes have a statistical significance of less than 5σ (see Table II). The $\rho(770)$ may decay to K^+K^- if its mass is larger than K^+K^- threshold, but its significance is 4.6σ . A P -wave π^0K^\pm system as an additional non-resonance contribution was tried and had a significance of 1.9σ . The variations to the $K^*(892)^\pm$ and $K_2^*(1430)^\pm$ signal yields by including these intermediate states are included as a systematic uncertainty.

TABLE I: The significance and number of events of each resonance under the best solution.

Decay	Fitted events	Significance(σ)
$K^*(892)^\pm K^\mp$	224 ± 21	26.5
$K_2^*(1430)^\pm K^\mp$	251 ± 22	21.0
$K^*(1680)^\pm K^\mp$	115 ± 20	11.1
$\rho^0(1700)\pi^0$	59 ± 10	8.7
$K^+K^-\pi^0$	721 ± 60	18.8

TABLE II: Significance for additional resonance.

Decay	Significance(σ)
$\rho^0(770)\pi^0$	4.63
$\rho^0(1450)\pi^0$	4.40
$\rho^0(1900)\pi^0$	1.13
$\rho^0(2150)\pi^0$	3.21
$\rho_3^0(1690)\pi^0$	1.84
$K^*(1410)^\pm K^\mp$	2.23
$K_2^*(1980)^\pm K^\mp$	2.14
$K_3^*(1780)^\pm K^\mp$	3.05
$K^*(2045)^\pm K^\mp$	3.26
non-resonance ($K^\mp\pi^0$)	1.89

For intermediate states around $K\pi$ invariant mass of 1.43 GeV, there are four established resonances, namely, $K_1(1400)$, $K^*(1410)$, $K_0^*(1430)$ and $K_2^*(1430)$; according to the spin-parity conservation, only $K_2^*(1430)$ and $K^*(1410)$ are allowed. If $K_2^*(1430)^\pm K^\mp$, which is

the best solution in the PWA, is replaced with $K^*(1410)^\pm K^\mp$, the fit fails to match the data, and the log-likelihood gets worse by 126, and the contribution from the $K^*(1410)$ is negligible. If $K^*(1410)^\pm K^\mp$ is taken in addition to $K_2^*(1430)^\pm K^\mp$ to the best solution, the log-likelihood only improves by 3.65, corresponding to a significance of 2.2σ .

The non-resonance decay $\psi' \rightarrow K^+ K^- \pi^0$ is indispensable in the fit, with a statistical significance of 19σ . We have tried to replace it with a broad resonance, such as $\rho(2150)\pi^0$. The fit fails to match the data, and the log-likelihood gets worse by 95. Note that the total number of fitted events 1370 ± 70 in Table I is larger than the number of net $K^+ K^- \pi^0$ events 917(=1158-241) due to the destructive interference among the included resonances.

The numbers of fitted events given in Table I are derived from numerical integration of the resultant amplitudes as done in Ref. [24]. The statistical errors are derived from the S distribution versus the number of fitted events; one standard deviation corresponds to the interval that produce a change of log-likelihood of 0.5. When performing the PWA fit to the data, the masses and widths of the intermediate states are fixed at the PDG values, and their errors quoted in the PDG are used to estimate the associated systematic errors.

Figure 6 depicts a comparison between the data and the best solution obtained from the PWA fit to the data. Here the projected $M_{K^+K^-}$ and $M_{\pi^0 K^\pm}$ mass distributions are shown. They are in general in a good agreement except for several points at the low $M_{K^+K^-}$ mass region. An additional $\rho(1450)\pi^0$ to the best solution in the PWA helps to improve the fit quality through destructive interference (see Fig. 7). The statistical significance of this additional mode is only about 3.2σ and it only brings a small difference in signal yields, 3.3% for $K^*(892)^\pm K^\mp$ and 0.4% for $K_2(1430)^*\pm K^\mp$. These yield differences are taken as a systematic uncertainties to account for additional resonance contributions to the low $M_{K^+K^-}$ mass region.

The goodness of the global fit is determined by calculating a χ_{all}^2 defined by

$$\chi_{\text{all}}^2 = \sum_{j=1}^5 \chi_j^2, \text{ with } \chi_j^2 = \sum_{i=1}^N \frac{(N_{ji}^{DT} - N_{ji}^{Fit})^2}{N_{ji}^{Fit}}, \quad (10)$$

where N_{ji}^{DT} and N_{ji}^{Fit} are the number of events in the i -th bin for the distribution of the j -th kinematic variable. If the measured values N_{ji}^{DT} are sufficiently large, then the χ_{all}^2 statistic follows the χ^2 distribution function with the number of degrees of freedom (ndf) equal to the total bins of histograms [27] minus the number of fitted parameters; and the individual

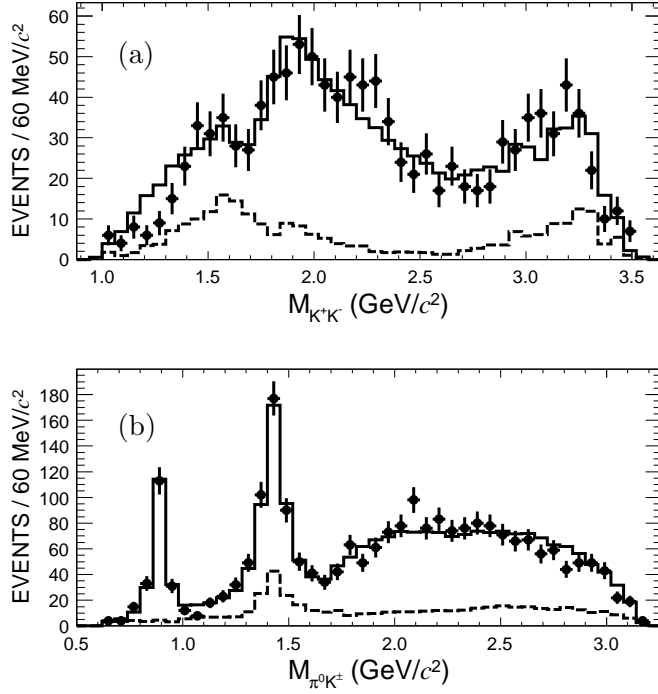


FIG. 6: The results of fit to (a) K^+K^- and (b) $\pi^0 K^\pm$ mass distributions for the data, where points with error bars are data and histograms are total fit results. The dashed histograms are the sum of the background sources, including QED and non- $K^+K^-\pi^0$ contributions.

χ_j^2 gives a qualitative measure of the goodness of the fit for each kinematic variable.

For the 3-body decay $\psi' \rightarrow K^+K^-\pi^0$, there are 5-independent variables, which are selected as the mass of the K^+K^- system ($M_{K^+K^-}$), the mass of the $\pi^0 K^\pm$ system ($M_{\pi^0 K^\pm}$), the polar angle for the π^0 (θ_{π^0}), the polar angle for the K^- (θ_{K^-}), and the azimuthal angle for the K^+ (ϕ_{K^+}), where the angles are defined in the ψ' rest frame. Figure 8 compares the angular distributions between the best fit solution and the data, and a good agreement can be observed. A sum of all these χ_j^2 values gives $\chi_{\text{all}}^2 = 147.70$, and the total number of degrees of freedom (126) is taken as the sum of the total number of bins having non-zero events minus the total number of parameters in the PWA fit. The global fit goodness χ_{all}^2/ndf is 1.2.

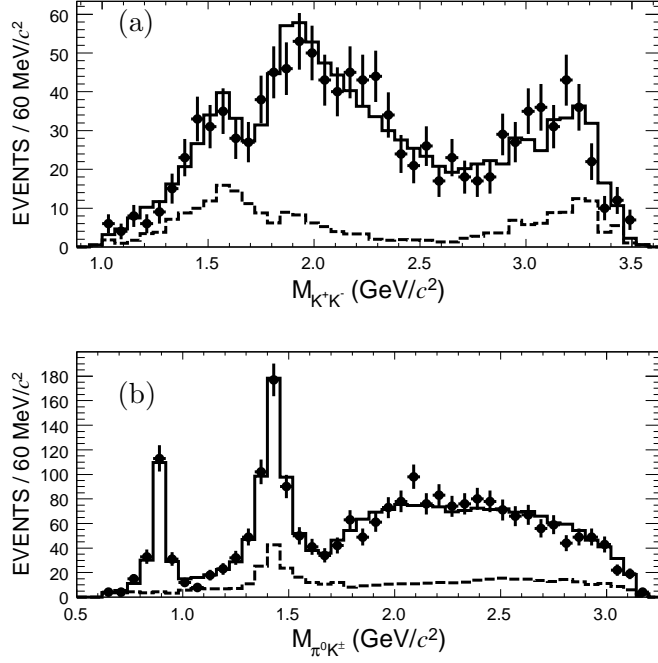


FIG. 7: The results of fit to (a) K^+K^- and (b) $\pi^0 K^\pm$ mass distributions for the data; where points with error bars are data; histograms denote total fit results with an additional mode of $\rho(1450)\pi^0$ being added to the best solution of the PWA fit (see Fig. 6). The dashed histograms are the sum of the background sources, including QED and non- $K^+K^-\pi^0$ contributions.

D. Branching fractions

Branching fractions for $\psi' \rightarrow K^*(892)^+K^- + c.c.$, $\psi' \rightarrow K_2^*(1430)^+K^- + c.c.$, and the inclusive decay $\psi' \rightarrow K^+K^-\pi^0$ (including all resonances) are calculated

$$\begin{aligned}
 Br(\psi' \rightarrow K^{*+}K^- + c.c.) &= \frac{N_{K^*}^{obs}}{\epsilon N_{\psi'} Br(K^{*+} \rightarrow K^+\pi^0) Br(\pi^0 \rightarrow \gamma\gamma)}, \\
 Br(\psi' \rightarrow K^+K^-\pi^0) &= \frac{N_{K^+K^-\pi^0}^{obs}}{\epsilon N_{\psi'} Br(\pi^0 \rightarrow \gamma\gamma)}.
 \end{aligned} \tag{11}$$

Here $Br(K^{*+} \rightarrow K^+\pi^0)$ is the branching fraction for $K^*(892)^+$ (33.23%) or $K_2^*(1430)^+$ (16.60%) resonances; $N_{K^*}^{obs}$ is the signal yield obtained from the PWA fit (224 ± 21 and 251 ± 22 for $K^*(892)$ and $K_2^*(1430)$, respectively); $N_{K^+K^-\pi^0}^{obs}$ is the net number of $K^+K^-\pi^0$ events (917 ± 37); $N_{\psi'} = (106 \pm 4) \times 10^6$ is the number of ψ' events[25]; and ϵ is the detection efficiency. To determine ϵ , the intensity from the amplitudes is used to weight both the complete set of generated MC events and the set which survives the selection procedure,

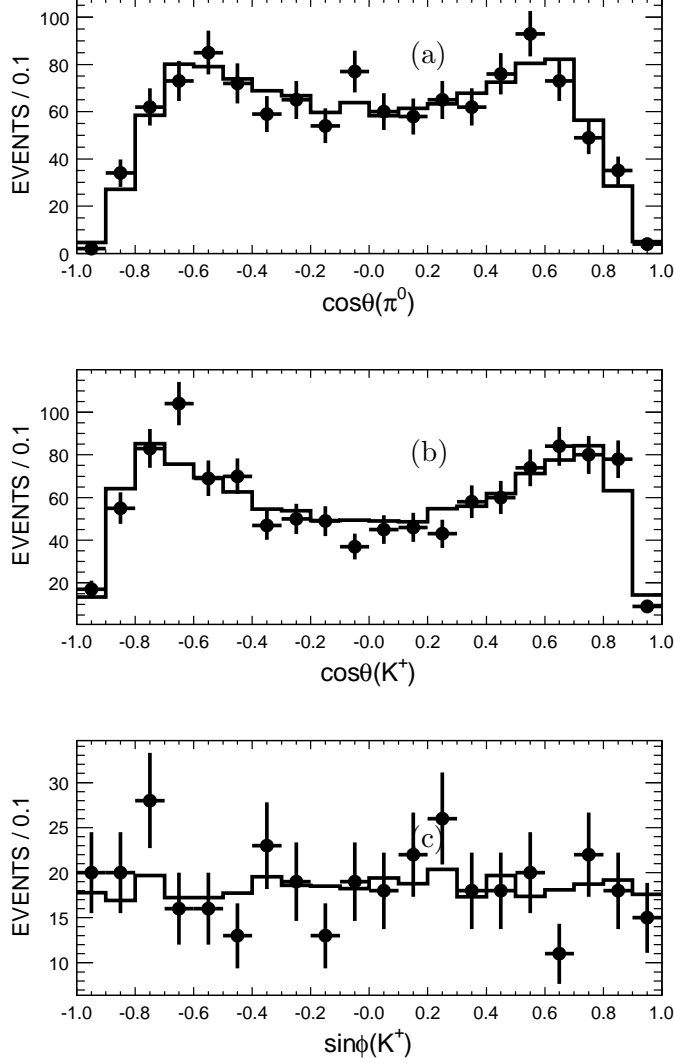


FIG. 8: The fit results of the angular distributions, where the points with error bars are data and histograms are the fit results. (a) $\cos\theta$ distribution for π^0 , (b) $\cos\theta$ distribution for K^+ , and (c) $\sin\phi$ distribution for K^+ , here the angles are defined in the ψ' rest frame.

and the ratio between these two weighted sets is taken as the detection efficiency.

The branching fractions are measured to be:

$$Br(\psi' \rightarrow \pi^0 K^+ K^-) = (4.07 \pm 0.16) \times 10^{-5}, \quad (12)$$

$$Br(\psi' \rightarrow K^*(892)^+ K^- + c.c.) = (3.18 \times 0.30) \times 10^{-5}, \quad (13)$$

$$Br(\psi' \rightarrow K_2^*(1430)^+ K^- + c.c.) = (7.12 \pm 0.62) \times 10^{-5}, \quad (14)$$

where the errors are only statistical.

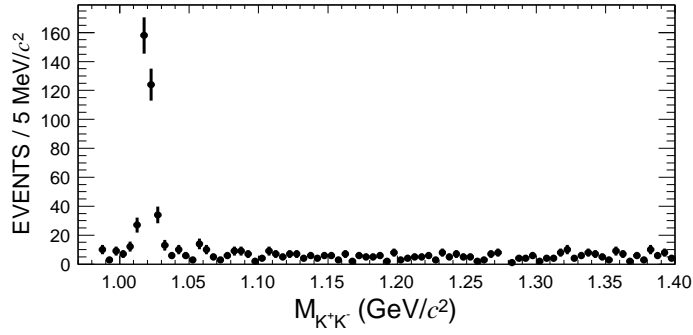


FIG. 9: The K^+K^- invariant mass selected in $\psi' \rightarrow \gamma\gamma K^+K^-$.

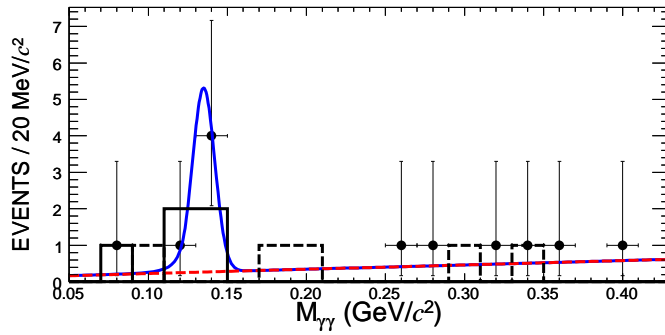


FIG. 10: (Color online) The invariant mass distribution of two photons in the selected $\psi' \rightarrow \phi\gamma\gamma$ events; the solid line shows a fit to π^0 ; the dashed line shows the fitted background and comparison to the backgrounds estimated with ϕ sideband (line histogram) and MC simulation (dashed histogram).

V. $\psi' \rightarrow \pi^0\phi$

The ϕ candidates for $\psi' \rightarrow \phi\pi^0$ are reconstructed using the two kaons selected in the decay $\psi' \rightarrow K^+K^-\gamma\gamma$. Figure 9 shows the invariant mass distribution of the two kaons, and a ϕ signal is clearly seen. The ϕ candidates are selected by requiring $|M_{K^+K^-} - m_\phi| < 10$ MeV/ c^2 , where $M_{K^+K^-}$ and m_ϕ are the invariant mass of the two kaons and the mass of the ϕ [5]. Background sources from the initial state radiation process $e^+e^- \rightarrow \gamma\phi$ are suppressed by requiring that the energy for the energetic photon is less than 1.6 GeV. Figure 10 shows the invariant mass distribution of the two photons after the ϕ selection criterion is applied. No significant π^0 signal is observed.

The number of observed events for $\psi' \rightarrow \pi^0\phi$ is obtained by fitting the mass distribution of

the two photons as shown in Fig. 10. The line shape of π^0 is taken from the MC simulation, and the background shape is taken as a first-order Chebychev polynomial function. The fit results are shown in Fig. 10 and the significance of π^0 signal is less than 3.0σ . The upper limit of observed π^0 events is estimated using the Bayesian approach to be $N^{up} = 6$ at the 90% confidence level.

The upper limit on the branching fraction for $\psi' \rightarrow \pi^0\phi$ is calculated with

$$Br(\psi' \rightarrow \pi^0\phi) < \frac{N^{up}}{\varepsilon N_{\psi'} Br(\pi^0 \rightarrow \gamma\gamma) Br(\phi \rightarrow K^+K^-)(1 - \sigma^{sys})}, \quad (15)$$

where $Br(\pi^0 \rightarrow \gamma\gamma)$ and $Br(\phi \rightarrow K^+K^-)$ are the branching fractions for $\pi^0 \rightarrow \gamma\gamma$ and $\phi \rightarrow K^+K^-$, respectively; $N_{\psi'} = (106 \pm 4) \times 10^6$ is the number of total ψ' decays; $\varepsilon = 35.63\%$ is the detection efficiency that was determined using MC events generated with the angular distribution $1 + \cos^2\theta$ for $\psi' \rightarrow \pi^0\phi$, where θ is the ϕ polar angle. $\sigma^{sys} = 5.8\%$ is the systematic error as listed in Table III. The upper limit of the branching fraction is $Br(\psi' \rightarrow \phi\pi^0) < 4.0 \times 10^{-7}$ at the 90% C.L.

VI. $\psi' \rightarrow \eta K^+ K^-$

A. Background analysis

Background sources for $\psi' \rightarrow \eta K^+ K^-$ are studied with the ψ' inclusive MC sample. The dominant background comes from $\psi' \rightarrow \gamma\gamma_{FSR} K^+ K^-$, where γ_{FSR} is a final-state radiation photon, $\psi' \rightarrow \gamma\chi_{c2}$, with $\chi_{c2} \rightarrow K^+ K^- \pi^0$ and $K^+ K^- \eta$. The MC simulation shows that the $M_{\gamma\gamma}$ mass distribution of sum of these events in the region of the η meson is a smooth and well modeled with a polynomial function.

Background events from QED processes are studied using events taken at $\sqrt{s} = 3.773$ GeV that are selected with the same criteria applied to the ψ' data. The signal yields are extracted with the same fit procedure used for the ψ' data. For $\eta\phi$, the contribution from the resonance decay $\psi(3770) \rightarrow \eta\phi$ is estimated to be 450 ± 112 events using the measured cross section $\sigma = 2.4 \pm 0.6$ pb [26]. After subtracting the resonance decays, the QED yield for the $e^+e^- \rightarrow \eta\phi$ at $\sqrt{s} = 3.773$ GeV is determined to be 268 ± 115 events. For $\eta K^+ K^-$, the observed events are considered to be exclusively from QED processes because the $\psi(3770) \rightarrow \eta K^+ K^-$ has not observed [5]. At the ψ' peak, the QED background sources

are estimated to be 16 ± 7 events for the $\eta\phi$ and 4 ± 1 events for the $\eta K^+ K^-$ according to the luminosity normalization. As a cross check, we use the data taken at $\sqrt{s} = 3.65$ GeV to determine a QED background of 25 ± 9 events. The difference between the two estimates is taken as a background uncertainty and included into systematic errors.

B. Fit results

We performed a two-dimensional unbinned fit to the scatter plot of $M_{K^+K^-}$ versus $M_{\gamma\gamma}$ distribution assuming that $M_{K^+K^-}$ and $M_{\gamma\gamma}$ are independent variables. Motivated by the structures seen in the $M_{K^+K^-}$ distribution, resonances including $\phi(1020)$, $\phi_3(1850)$ and $\phi(2170)$ are added to the fit. The fit function includes the line shapes describing the two-body decays $\eta\phi(1020)$, $\eta\phi_3(1850)$, $\eta\phi(2170)$, the non-resonant decay $\eta K^+ K^-$, and the background. The η line shape is obtained from a MC simulation; the line shapes for the $\phi(1020)$, $\phi_3(1850)$ and $\phi(2170)$ are described as non-relativistic Breit-Wigner functions with their masses and widths fixed to the PDG values. The Breit-Wigner function of all the ϕ states are convolved with a detector resolution function. The background shapes for the $M_{\gamma\gamma}$ and the $M_{K^+K^-}$ mass distributions are taken as first- and second-order polynomials, respectively.

The fit results after projecting to the mass distributions are shown in Figs. 11 and 12. The signal yield for the $\psi' \rightarrow \eta\phi$ channel is 232 ± 16 events. Adding the $\phi_3(1850)$ and $\phi(2170)$ resonances to the fit improves the fit quality with a statistical significance of 3.8σ for the $\phi_3(1850)$, and 3.1σ for the $\phi(2170)$. The goodness of the fit is $\chi^2/ndf = 0.32(0.43)$ for the $M_{\gamma\gamma}(M_{K^+K^-})$ distribution. The yields of $\eta\phi_3(1850)$ and $\eta\phi(2170)$ plus the contribution from the non-resonance decay $\psi' \rightarrow \eta K^+ K^-$ totals 288 ± 27 events. After subtracting the QED background, the net signals are 216 ± 16 events for $\psi' \rightarrow \eta\phi$, and 284 ± 27 events for $\psi' \rightarrow \eta K^+ K^-$.

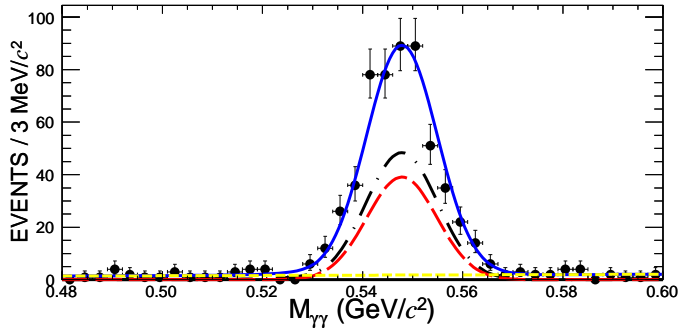


FIG. 11: (Color online) Fit results projected to the two-photon invariant mass distribution $M_{\gamma\gamma}$. Dots with error bars are data. The solid line is the total fit results, and the dashed-dotted and long-dashed lines are the results of $\eta\phi$ and ηKK contributions, respectively. The short-dashed line is the background contribution.

C. Branching fractions

Branching fractions are calculated from the relations

$$Br(\psi' \rightarrow \eta K^+ K^-) = \frac{N_{\eta KK}^{obs}}{\varepsilon_{\eta KK} N_{\psi'} Br(\eta \rightarrow \gamma\gamma)}, \quad (16)$$

$$Br(\psi' \rightarrow \eta\phi) = \frac{N_{\eta\phi}^{obs}}{\varepsilon_{\eta\phi} N_{\psi'} Br(\eta \rightarrow \gamma\gamma) Br(\phi \rightarrow K^+ K^-)}. \quad (17)$$

Here $N_{\eta KK}^{obs} = 284 \pm 27$ and $N_{\eta\phi}^{obs} = 216 \pm 16$ are the numbers of net signal events; $Br(\eta \rightarrow \gamma\gamma)$ and $Br(\phi \rightarrow K^+ K^-)$ are the branching fractions for the $\eta \rightarrow \gamma\gamma$ and $\phi \rightarrow K^+ K^-$ decays, respectively; $\varepsilon_{\eta KK} = 22.10\%$ and $\varepsilon_{\eta\phi} = 33.53\%$ are the detection efficiencies determined from MC simulations, whose angular distributions match the data; $\varepsilon_{\eta KK}$ is a weighted average for $\psi' \rightarrow \eta K^+ K^-$, $\eta\phi_3(1850)$ and $\eta\phi(2170)$. The branching fractions are calculated to be $Br(\psi' \rightarrow \eta KK) = (2.97 \pm 0.28) \times 10^{-5}$ and $Br(\psi' \rightarrow \eta\phi) = (3.08 \pm 0.29) \times 10^{-5}$, where the errors are only statistical.

VII. SYSTEMATIC ERRORS

The systematic errors in the branching fraction measurement originated from following sources are considered:

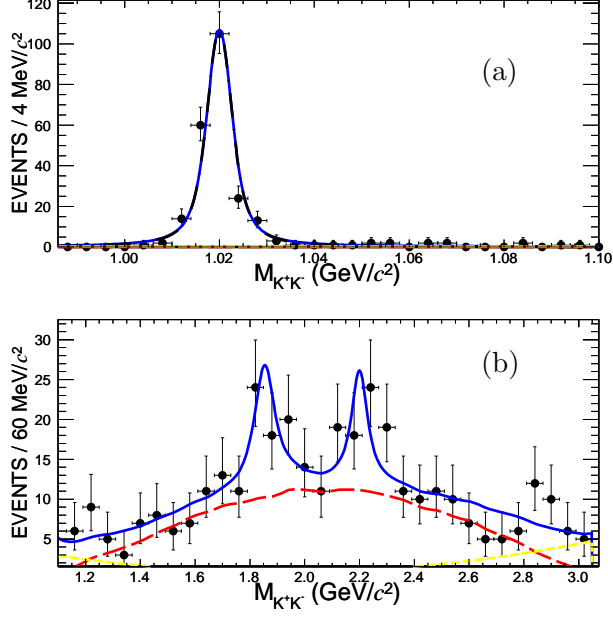


FIG. 12: (Color online) Fit results projected to the K^+K^- invariant mass distribution $M_{K^+K^-}$ for (a) the $\phi(1020)$ resonance, (b) the $\phi(1850)$ and $\phi(2170)$ resonances. Dots with error bars are data. The solid lines are the total fit results, and the dashed-dotted and long-dashed lines are the results of $\eta\phi$ and ηK^+K^- , respectively. The short-dashed line is the background contribution.

1. photon efficiency

The soft and hard photon efficiencies are studied using $\psi' \rightarrow \pi^0\pi^0 J/\psi$, $J/\psi \rightarrow e^+e^-$, $\mu^+\mu^-$ and $J/\psi \rightarrow \rho\pi \rightarrow \pi^+\pi^-\pi^0$ decays. The difference in the photon efficiency between the MC simulation and data is 1%, which is taken as a systematic uncertainty.

2. kaon tracking and PID efficiency

The uncertainties of kaon tracking and PID efficiency are studied using a sample of $J/\psi \rightarrow K^*(892)^0 K_S^0 + c.c. \rightarrow K_S^0 K^+ \pi^- + c.c. \rightarrow K^+ \pi^- \pi^+ \pi^- + c.c.$ events as done in [19]. The uncertainties for both tracking and PID are determined to be 1% per track.

3. Number of ψ' events

The number of ψ' events is determined using its hadronic decays. The uncertainty is 4% [25].

4. branching fractions

The uncertainties of branching fractions for $K^*(892)^\pm/K_2(1430)^\pm \rightarrow K^\pm\pi^0$, $\pi^0/\eta \rightarrow$

$\gamma\gamma$ and $\phi \rightarrow K^+K^-$ are taken from the world average values [5].

5. kinematic fit

The differences between the MC simulation and data in the χ^2 distribution of the kinematic fit arise mainly due to inconsistencies in the charged track parameters. The kaon track parameters in the MC simulation are corrected by smearing them to match the data. The difference in the detection efficiency between with and without making a correction to the MC is taken as a systematic error. The uncertainties are listed in Table III.

6. the π^0 mass window

The uncertainty due to the π^0 mass window is studied by comparing the π^0 selection efficiency obtained in the MC and the data. The uncertainty is 1.1%.

7. fit uncertainty

The fit uncertainties in the ηK^+K^- and $\eta\phi$ modes are determined by changing the fit range and background shapes. The fit range of two photons is changed to be [460, 620] MeV/ c^2 or [470, 670] MeV/ c^2 . It is estimated to be 3.6% (0.6%) for ηK^+K^- ($\eta\phi$). The background function is changed from 1st-order to 3rd-order polynomials. The uncertainties due to the background shapes are 1.6% and 0.4% for ηK^+K^- and $\eta\phi$, respectively.

8. QED backgrounds

The QED background subtracted from $\eta\phi$ is determined with the data taken at $\sqrt{s} = 3.773$ GeV and at $\sqrt{s} = 3.65$ GeV. The difference in the number of QED events between these two samples is 4.5%, which is taken as the QED background associated uncertainty.

9. additional resonances for ηK^+K^-

The existence of $\phi_3(1850)$ and $\phi(2170)$ intermediate states in ηK^+K^- cannot be determined due to the low statistics. The difference between the branching fractions determined by including and excluding these two resonances is taken as a systematic error of 4.0%.

All above systematic errors are listed in Table III.

For $K^+K^-\pi^0$, the uncertainties from the PWA fit are listed below:

1. Breit-Wigner form

The uncertainty due to the resonance line shape is evaluated by using the Breit-Wigner function with a width $\Gamma(s)$ dependent on the energy, i.e.

$$\Gamma(s) = \Gamma_0 \frac{m^2}{s} \left[\frac{p(s)}{p(m^2)} \right]^{2L+1}, \quad (18)$$

where s is the resonance mass squared; m and Γ_0 are the nominal mass and width, respectively; $p(s)$ is the magnitude of resonance momentum; L is the angular momentum for the ψ' decays into a two-body final state. The differences between the fit yields determined with a constant and an energy-dependent width are taken as systematic errors. They are evaluated to be 0.1% and 0.9% for the $K^*(892)$ and $K_2^*(1430)$, respectively.

2. additional resonances

The uncertainties from additional resonances, listed in Table II, are determined by adding them to the best solution of PWA fit one-by-one. The differences between the fit yields determined with and without the additional resonance are taken as systematic errors. For the non-resonant mode $\psi' \rightarrow K^+K^-\pi^0$, the uncertainty due to the P -wave K^+K^- system in the PWA fit is evaluated by replacing it with a P -wave $K\pi$ system. The difference in the fit yields is taken as a systematic error.

3. non- $K^+K^-\pi^0$ background

The number of non- $K^+K^-\pi$ background events is obtained from a π^0 -sideband analysis and an exclusive MC simulation. The difference in the signal yields corresponding to one standard deviation of this background is taken as a systematic error.

4. the QED background

The QED background used at $\sqrt{s} = 3.686$ GeV is produced via a MC simulation with amplitude information obtained from a PWA fit to the data taken at $\sqrt{s} = 3.773$ GeV. The uncertainty is estimated by replacing this QED background with the continuum data taken at $\sqrt{s} = 3.65$ GeV. The difference of the fitted yields between these two approaches are 0.8% and 9.9% for $K_2^*(1430)$ and $K^*(892)$, respectively, and used as systematic uncertainties.

5. uncertainty of $K^*(1680)$ and $\rho(1700)$ widths

The decay widths of $K^*(1680)$ and $\rho(1700)$ have large uncertainties; the world average values are $\Gamma_{K^*(1680)} = 322 \pm 110$ MeV and $\Gamma_{\rho(1700)} = 250 \pm 100$ MeV [5]. The signal yields were re-obtained using widths that are changed by one standard deviation with respect to the nominal value. The differences in signal yields between these two methods are taken as systematic errors.

6. uncertainties of masses and widths for the $K^*(892)$ and $K^*(1430)$

In the PWA fit, the masses and widths for the $K^*(892)$ and $K^*(1430)$ are fixed to the world average values. The differences in fit yields obtained by changing these parameters by one standard deviation are taken as systematic errors.

All systematic errors from the PWA fit are listed in Table IV.

Combining the systematic uncertainties from the PWA fit and the $\pi^0 K^+ K^-$ event selection gives total systematic errors of ${}_{-9.8}^{+8.3}\%$ and ${}_{-8.1}^{+15.6}\%$ for $\psi' \rightarrow K^*(892)^+ K^- + c.c.$ and $K_2^*(1430)^+ K^- + c.c.$, respectively.

VIII. SUMMARY AND DISCUSSION

Using $(106 \pm 4) \times 10^6$ ψ' decays accumulated with BESIII, we measured branching fractions for the $\psi' \rightarrow K^*(892)^+ K^- + c.c.$, $K^*(1430)^+ K^- + c.c.$, $\eta\phi$, $\pi^0\phi$, $\pi^0 K^+ K^-$, and $\eta K^+ K^-$ decays. The helicity forbidden decay $\psi' \rightarrow K_2^*(1430)^+ K^- + c.c.$ is observed for the first time, and its branching fraction is measured; this reflects a violation of the helicity selection rule [10]. Table V gives an overview of our results with comparisons with BESII- and CLEO-measurements and world average values. The precision of our measurements is better for all the modes, including a tightened upper limit for $\pi^0\phi$. In the measurement of $Br(\psi' \rightarrow \pi^0 K^+ K^-)$, all intermediate states are included in the branching fraction, while for the measurement of $Br(\psi' \rightarrow K^+ K^- \eta)$, $\psi' \rightarrow \eta\phi$ is excluded. The measurements of branching fractions for the $\psi' \rightarrow K^*(892)^+ K^- + c.c.$ and $\eta\phi$ are consistent with BESII results within 1σ , and CLEO measurements within 2σ .

Using the world average values of branching fractions for J/ψ decays, the Q_h values are calculated and listed in Table V. For $\psi' \rightarrow K^*(892)^+ K^- + c.c.$ and $\eta\phi$, the Q_h values significantly deviate from the expected value of 12%.

TABLE III: Summary of all systematic errors (%).

Items	$\pi^0 K^+ K^-$	$K^{*\pm} K^\mp$	$K_2^{*\pm} K^\mp$	$\eta K^+ K^-$	$\eta\phi$	$\pi^0\phi$
Photon efficiency	2	2	2	2	2	2
π^0 mass cut	1.1	1.1	1.1	—	—	—
Kaon tracking	2	2	2	2	2	2
PID	2	2	2	2	2	2
Kinematic fitting	1.9	3.2	4.3	2.1	1.7	2.1
Number of ψ' decays	4	4	4	4	4	4
Background shape	—	—	—	1.6	0.4	—
Fitting range	—	—	—	3.6	0.6	—
$Br[K_J^*] \rightarrow \pi^0 K$	—	—	2.4	—	—	—
$Br[P \rightarrow \gamma\gamma]$	—	—	—	0.5	0.5	—
$Br[\phi \rightarrow KK]$	—	—	—	—	1.2	1.2
QED background	—	—	—	—	4.5	—
Additional states	—	—	—	4	—	—
Total	6.3	6.9	6.2	8.0	7.3	5.8

TABLE IV: Summary of systematic uncertainties from the PWA (%).

Sources	$K^*(892)^\pm K^\mp$	$K_2^*(1430)^\pm K^\mp$
Breit-Wigner	-0.1	+0.9
Additional states	+5.2 -6.9	+10.3 -4.6
Non- $K^+ K^- \pi$ background	+1.4 -1.6	+1.2 -1.0
QED background	-0.8	+9.9
$K^*(1680)$, $\rho(1700)$ width	+0.5 -1.1	0 -2.0
$K^*(892)$, $K_2^*(1430)$ Mass and width	+0.4 -0.4	+0.3 0
Total	+5.4 -7.3	+14.3 -5.1

Acknowledgments

The BESIII collaboration thanks the staff of BEPCII and the computing center for their hard efforts. This work is supported in part by the Ministry of Science and Technology of

TABLE V: Summary of the measured branching fractions compared with PDG [5] values, together with CLEO [3] and BESII [4] measurements. The upper limit is given at the 90% confidence level. The first error is statistical, and the second error is systematic. Here ϵ , N^{obs} , and Br denote the detection efficiency, the number of observed events, and the branching fraction, respectively. The variable Q_h is defined by Eq. (1).

Mode($\psi' \rightarrow$)	$\epsilon(\%)$	N^{obs}	Br($\times 10^{-5}$)	Q_h (%)	PDG($\times 10^{-5}$)	CLEO($\times 10^{-5}$)	BESII($\times 10^{-5}$)
$\pi^0 K^+ K^-$ (inclusive)	21.52	917 \pm 37	4.07 \pm 0.16 \pm 0.26	—	< 8.9 [2]	—	—
$K^*(892)^+ K^- + c.c.$	20.25	224 \pm 21	3.18 \pm 0.30 $^{+0.26}_{-0.31}$	0.62 \pm 0.09	1.7 $^{+0.8}_{-0.9}$	1.3 \pm 1.0 \pm 0.3	2.9 \pm 1.3 \pm 0.4
$K_2^*(1430)^+ K^- + c.c.$	20.28	251 \pm 22	7.12 \pm 0.62 $^{+1.13}_{-0.61}$	> 2	—	—	—
$\eta K^+ K^-$ ($\eta\phi$ excluded)	22.10	284 \pm 27	3.08 \pm 0.29 \pm 0.25	—	< 13	< 13	—
$\eta\phi$	33.53	216 \pm 16	3.14 \pm 0.23 \pm 0.23	4.19 \pm 0.61	2.8 $^{+1.0}_{-0.8}$	2.0 \pm 1.1 \pm 0.4	3.3 \pm 1.1 \pm 0.5
$\pi^0\phi$	35.63	<10	<0.04	—	< 0.4	0.7	0.4

China under Contract No. 2009CB825200; National Natural Science Foundation of China (NSFC) under Contracts Nos. 10625524, 10821063, 10825524, 10835001, 10935007; Joint Funds of the National Natural Science Foundation of China under Contract No. 11079008; the Chinese Academy of Sciences (CAS) Large-Scale Scientific Facility Program; CAS under Contracts Nos. KJCX2-YW-N29, KJCX2-YW-N45; 100 Talents Program of CAS; Istituto Nazionale di Fisica Nucleare, Italy; Siberian Branch of Russian Academy of Science, joint project No 32 with CAS; U. S. Department of Energy under Contracts Nos. DE-FG02-04ER41291, DE-FG02-91ER40682, DE-FG02-94ER40823; U.S. National Science Foundation; University of Groningen (RuG) and the Helmholtzzentrum fuer Schwerionenforschung GmbH (GSI), Darmstadt; WCU Program of National Research Foundation of Korea under Contract No. R32-2008-000-10155-0. This paper is also supported by the NSFC under Contract Nos. 10979038, 10875113, 10847001, 11005115; Innovation Project of Youth Foundation of Institute of High Energy Physics under Contract No. H95461B0U2.

[1] T. Appelquist and H. D. Politzer, Phys. Rev. Lett. **34**, 43 (1975);

A. De Rujula and S. L. Glashow, Phys. Rev. Lett. **34**, 46 (1975).

[2] M. E. B. Franklin *et al.* (Mark II Collaboration), Phys. Rev. Lett. **51**, 963 (1983).

- [3] N. E. Adam *et al.* (CLEO Collaboration), Phys. Rev. Lett. **94**, 012005 (2005).
- [4] M. Ablikim *et al.* (BES Collaboration), Phys. Lett. B **619**, 247 (2005);
M. Ablikim *et al.* (BES Collaboration), Phys. Lett. B **614**, 37 (2005);
M. Ablikim *et al.* (BES Collaboration), Phys. Rev. D **70**, 112003 (2004);
M. Ablikim *et al.* (BES Collaboration), Phys. Rev. D **70**, 112007 (2004).
- [5] K. Nakamura *et al.* (Particle Data Group), Phys. Rev. D **86**, 010001 (2012).
- [6] N. Brambilla *et al.* (Quarkonium Working Group), Eur. Phys. J. C **71**, 1534 (2011);
Y. F. Gu and X. H. Li, Phys. Rev. D **63**, 114019 (2001);
Q. Wang, G. Li, and Q. Zhao, Phys. Rev. D **85**, 074015 (2012) [arXiv:1201.1681[hep-ph]];
X. -H. Mo, C. -Z. Yuan and P. Wang, High Energy Physics and Nuclear Physics **31**, 686
(2007) [hep-ph/0611214].
- [7] V. L. Chernyak and A. R. Zhitnitsky, Nucl. Phys. B **201**, 492 (1982); B **214**, 547(E) (1983).
- [8] S. J. Brodsky and G. P. Lepage, Phys. Rev. D **24**, 2848 (1981).
- [9] M. Ablikim *et al.* (BESIII Collaboration), Phys. Rev. Lett. **107**, 092001 (2011).
- [10] Xiao-Hai Liu and Qiang Zhao, Phys. Rev. D **81**, 014017 (2010).
- [11] Q. Wang, G. Li and Q. Zhao, Phys. Rev. D **85**, 074015 (2012).
- [12] M. Ablikim *et al.* (BESIII Collaboration), Nucl. Instrum. Methods Phys. Res., Sect. A **614**,
345 (2010).
- [13] D. S. Asner *et. al.*, Int. J. Mod. Phys. A **24**, Supp.(2009).
- [14] Z. Y. Deng *et al.*, High Energy Physics and Nuclear Physics **30**, 371 (2006).
- [15] S. Jadach, B. F. L. Ward, and Z. Was, Comput. Phys. Commun. **130**, 260 (2000); Phys. Rev.
D **63**, 113009 (2001).
- [16] R. G. Ping, Chin. Phys. C **32**, 599 (2008).
- [17] J. C. Chen, G. S. Huang, X. R. Qi, D. H. Zhang, and Y. S. Zhu, Phys. Rev. D **62**, 034003
(2000).
- [18] W. D. Li *et al.*, in Proceedings of CHEP06, Mumbai, India, 2006 edited by Sunanda Banerjee
(Tata Institute of Fundamental Research , Mumbai, 2006).
- [19] M. Ablikim *et al.* (BESIII Collaboration), Phys. Rev. D **83**, 112005 (2011).
- [20] J. Z. Bai *et al.* (BES Collaboration), Phys. Rev. D **68**, 052003 (2003);
M. Ablikim *et al.* (BES Collaboration), Phys. Lett. B **598**, 149 (2004);
M. Ablikim *et al.* (BES Collaboration), Phys. Lett. B **607**, 243 (2005).

- [21] B. S. Zou and D. V. Bugg, *Eur. Phys. J. A* **16**, 537 (2003).
- [22] I. Silin, CERN Program Library D **510**, 1971.
- [23] A. V. Anisovich *et al.*, *Phys. Lett. B* **491**, 40 (2000).
- [24] M. Ablikim *et al.* (BES Collaboration), *Phys. Rev. D* **72**, 092002 (2005).
- [25] M. Ablikim *et al.* (BESIII Collaboration), *Phys. Rev. D* **81**, 052005 (2010).
- [26] G. S. Adams *et al.* (CLEO Collaboration), *Phys. Rev. D* **73**, 012002 (2006).
- [27] In a histogram, bins with event entries less than 10 are combined as one bin.